
Title	Digital quantum simulation of the spin-boson model under Markovian open-system dynamics
Author(s)	Andreas Burger, Leong Chuan Kwek & Dario Poletti

Copyright © 2022 The Author(s) & MDPI

This is the published version of the following article:

Burger, A., Kwek, L. C., & Poletti, D. (2022). Digital Quantum Simulation of the Spin-Boson Model under Markovian Open-System Dynamics. *Entropy*, 24, Article 1766.

<https://doi.org/10.3390/e24121766>

Article

Digital Quantum Simulation of the Spin-Boson Model under Markovian Open-System Dynamics

Andreas Burger^{1,2,3,*}, Leong Chuan Kwek^{3,4,5}  and Dario Poletti^{2,3,4,6,7} 

- ¹ Faculty of Physics, Ludwig-Maximilians-Universität Munich, Geschwister-Scholl-Platz 1, 80539 Munich, Germany
 - ² Science, Mathematics and Technology Cluster, Singapore University of Technology and Design, Singapore 487372, Singapore
 - ³ Centre for Quantum Technologies, National University of Singapore, Singapore 117543, Singapore
 - ⁴ National Institute of Education and Institute of Advanced Studies, Nanyang Technological University, Singapore 637616, Singapore
 - ⁵ MajuLab, CNRS-UNS-NUS-NTU International Joint Research Unit, Singapore 117543, Singapore
 - ⁶ EPD Pillar, Singapore University of Technology and Design, 8 Somapah Road, Singapore 487372, Singapore
 - ⁷ The Abdus Salam International Centre for Theoretical Physics, Strada Costiera 11, 34151 Trieste, Italy
- * Correspondence: andreas.burger@physik.uni-muenchen.de

Abstract: Digital quantum computers have the potential to simulate complex quantum systems. The spin-boson model is one of such systems, used in disparate physical domains. Importantly, in a number of setups, the spin-boson model is open, i.e., the system is in contact with an external environment which can, for instance, cause the decay of the spin state. Here, we study how to simulate such open quantum dynamics in a digital quantum computer, for which we use an IBM hardware. We consider in particular how accurate different implementations of the evolution result as a function of the level of noise in the hardware and of the parameters of the open dynamics. For the regimes studied, we show that the key aspect is to simulate the unitary portion of the dynamics, while the dissipative part can lead to a more noise-resistant simulation. We consider both a single spin coupled to a harmonic oscillator, and also two spins coupled to the oscillator. In the latter case, we show that it is possible to simulate the emergence of correlations between the spins via the oscillator.

Keywords: quantum computing; NISQ; open system



Citation: Burger, A.; Kwek, L.C.; Poletti, D. Digital Quantum Simulation of the Spin-Boson Model under Markovian Open-System Dynamics. *Entropy* **2022**, *24*, 1766. <https://doi.org/10.3390/e24121766>

Academic Editor: Rosario Lo Franco

Received: 7 November 2022

Accepted: 29 November 2022

Published: 2 December 2022

Publisher's Note: MDPI stays neutral with regard to jurisdictional claims in published maps and institutional affiliations.



Copyright: © 2022 by the authors. Licensee MDPI, Basel, Switzerland. This article is an open access article distributed under the terms and conditions of the Creative Commons Attribution (CC BY) license (<https://creativecommons.org/licenses/by/4.0/>).

1. Introduction

A natural application of quantum computers is the simulation of quantum systems [1,2]. Furthermore, most hardware realizations of quantum computers implement the qubit. A prevalent qubit-based quantum system is the spin system. Existing quantum computers are based on unitary quantum circuits. Consequently, there has been a plethora of research on closed quantum systems [3–6]. Amongst the spin models, an important class is the spin-boson problem, where one or more spins are coupled to several bosonic degrees of freedom. These models possess rich many-body physics and they can model realistic coupling between electron transfer and protein motion or a solvent [7–11].

In recent years, NISQ computers [12,13] have offered a new perspective on the implementations on digital devices, leading to an explosion of activities. Not all computing tasks are amenable to quantum processing. Classical optimization can often perform better than quantum algorithms. The challenges of device-induced noise have led to the popularity of hybrid quantum-classical variational algorithms (VQA) that split the workload between a quantum and a classical processor. These techniques are ideally suited for the evaluation of different quantities such as eigenstates [14], general quantum approximate optimization algorithms [15], off-diagonal elements of matrices [16] and more [13]. Importantly, new error mitigation approaches have also been proposed [17–19]. VQA has been applied to boson-spin systems or its equivalents [20–22]. Regarding open systems, different VQA approaches

have been tested. They include approaches based on imaginary time evolution [23,24], stochastic Schrödinger Equation [25], variational quantum eigensolvers to reach steady states [26,27], and the quantum-assisted simulator without a classical-quantum feedback loop [28]. Mapping bosonic problems to quantum circuits has been laid out in [29–31], while a recent implementation of spin-boson models can be found in [6].

Simulating open quantum systems entirely on digital quantum computers has primarily focused on two-level systems. The amplitude damping channel has been implemented with a unitary dilation of the Kraus operators [32], using uniformly controlled gates [33,34], and with the amplitude damping circuit [2,35]. Larger systems have been realized using a linear combination of unitary matrices [36,37] and modified stochastic Schrödinger equation methods [38]. In [25], the authors proposed a hybrid classical-quantum variational approach to simulate generic Markovian open quantum systems.

Our aim is to simulate the open dynamics of a spin-boson model coupled to a dissipative channel on a digital quantum computer. We do this by mapping the bosonic modes to qubits, Trotterizing the unitary evolution, and modeling the dissipative portion via repeated collisions with a reset auxiliary qubit [35,39,40]. In doing so, we focus on using different noise levels in the quantum computer, from the value in current hardware, to 1% of it. With this in mind, we study how different implementations of the simulation perform in presence of different noise levels.

The paper is organized as follows. In Section 2.1, we introduce the open spin-boson model and lay out the circuit implementation. In Section 2.2, we describe the circuit implementation of the unitary and dissipative evolutions. We then detail our use of quantum hardware and noise-related limitations of the devices in Section 2.3. Our results are presented in Section 3. We quantify the error stemming from approximations in the model, and for different magnitudes of noise in the device. We study the optimal time-step-sizes and dissipative rates in terms of fidelity. Finally, we increase the system size to two spins and investigate whether it is possible to observe rising correlations amongst the spins.

2. Method

2.1. Model

We consider N_S non-interacting spins coupled to a single harmonic oscillator, as well as to a bath, as can be seen in Figure 1. The closed system is governed by the quantum Rabi Hamiltonian [41–43], which describes the ultra-strong coupling regime, where the usual rotating wave approximation breaks down and the counter-rotating term can no longer be neglected [44–46].

$$\hat{H}_{SB} = \hbar\omega\hat{a}^\dagger\hat{a} + \sum_{i=1}^{N_S} \frac{1}{2}(h\hat{\sigma}_k^z + \epsilon\hat{\sigma}_k^x) + \lambda\hat{\sigma}_k^x(\hat{a}^\dagger + \hat{a}), \tag{1}$$

Experimentally, the ultra-strong coupling regime has been investigated in circuit QED [47–52], trapped ions [53], photonic systems [54], and semiconductors [55,56].

In Equation (1), \hat{a}^\dagger and \hat{a} , respectively, create and destroy one excitation in the harmonic oscillator while $\hat{\sigma}_k^x = \hat{\sigma}_k^+ + \hat{\sigma}_k^-$ and $\hat{\sigma}_k^z$ are Pauli operators acting on the spin(s). h is the local magnetic field in the z direction while ϵ is a field in the x direction. λ is the magnitude of the coupling between the spins and the harmonic oscillator, with frequency ω . In the following, we will work in units such that $h = \hbar = 1$.

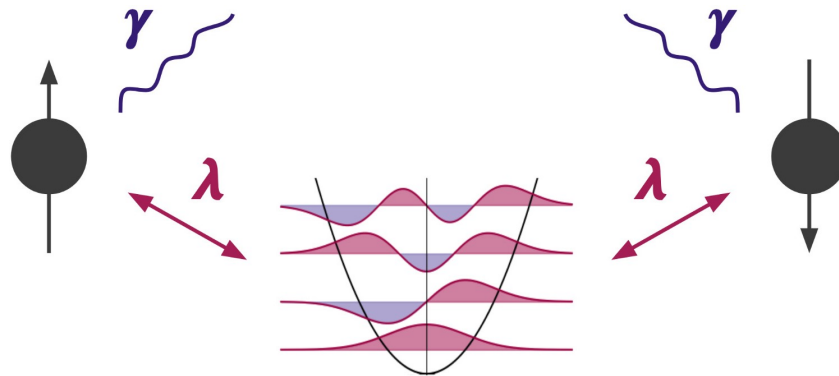


Figure 1. Depiction of the model described by Equations (1) and (2) for a number of spins $N_S = 2$. The two spin sites are coupled to one harmonic oscillator of frequency ω via coupling parameter λ . Each of the spins dissipates independently into the environment at a rate of γ .

The dissipative part of the dynamics is here described by a Markovian master equation in Gorini–Kossakovski–Sudarshan–Lindblad form [57,58]

$$\frac{d\hat{\rho}}{dt} = -\frac{i}{\hbar}[\hat{H}_{SB}, \hat{\rho}] + \gamma \sum_k (2\hat{L}_k \hat{\rho} \hat{L}_k^\dagger - \{\hat{L}_k^\dagger \hat{L}_k, \hat{\rho}\}) \tag{2}$$

with the amplitude damping channel $\hat{L}_k = |\downarrow\rangle_k \langle\uparrow|$ acting on the k -th spin and γ being the decay rate. $|\downarrow\rangle$ represents the vacuum state, whereas $|\uparrow\rangle$ represents the excited state of the spin.

Equation (2) describes a setup where loss from imperfections in the cavity is negligible compared to the spins emissions. In these systems, undesired decay transitions can include the emission of frequencies which are suppressed in the cavity and are thus effectively lost [59–61].

2.2. Circuit Implementation

In this section, we describe how we implement the evolution governed by Equations (1) and (2) in a quantum circuit.

2.2.1. Encoding of the Hamiltonian

We map the spin and bosonic operators in \hat{H}_{SB} to Pauli operators, and Trotterize the unitary $e^{-i\hat{H}_{SB}t}$. The spin part is trivially mapped to qubits. For the bosonic subspace and operators, we use a d-level-to-qubit mapping with Gray Code as the integer-to-bit encoding, as described in [31,62]. We give more details on the mapping to Q_B qubits in Appendix A.

2.2.2. Trotterization of Unitary

To implement the unitary evolution operator $U = e^{-i\hat{H}_{SB}t}$, we consider the first-order U_1 and second-order U_2 Suzuki–Trotter product formulas [63,64]

$$U_1 = (e^{-ih_1\Delta t} e^{-ih_2\Delta t} \dots e^{-ih_N\Delta t})^{\frac{t}{\Delta t}} \tag{3}$$

$$U_2 = (e^{-ih_1\frac{\Delta t}{2}} \dots e^{-ih_N\frac{\Delta t}{2}} e^{-ih_N\frac{\Delta t}{2}} \dots e^{-ih_1\frac{\Delta t}{2}})^{\frac{t}{\Delta t}} \tag{4}$$

where h_k are N different, non-commuting, terms of the Hamiltonian after encoding and $\Delta t = t/N$. The individual exponentials of Pauli strings $e^{-ih_k\Delta t}$ are then implemented via the CNOT-staircase [2,3], which is taken care of by Qiskit [65]. See Equations (A2) and (A3) in Appendix A for more details on h_k .

2.2.3. Collisional Model

We model the local master equation, namely Equation (2), via repeated collisions [39,66]. Figure 2 gives a depiction of a single collision. We consider the spin qubit s , and auxiliary qubit a and where a controlled- $R_Y(\theta)$ (rotation around y axis) is followed by a controlled-NOT and a reset of the auxiliary qubit, see Appendices C and D for more details. To reproduce Equation (2) we use $\theta = \arcsin(\sqrt{1 - e^{-\gamma t}})$ [2].

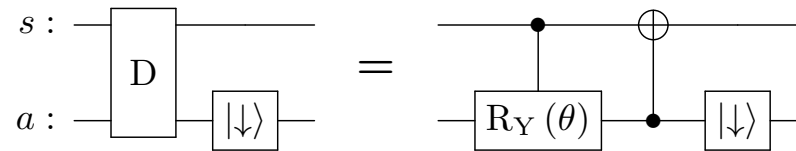


Figure 2. Circuit implementation of the dissipative part of the circuit, D , which represent a single collision to model Equation (2). s is the qubit representing the spin while a represents the auxiliary qubit.

2.2.4. Integration of Dissipative and Unitary Part

To integrate the step of Figure 2 in the main circuit, we employ a first-order Suzuki–Trotter decomposition which alternates between the unitary and the dissipative parts. In Figure 3a, we depict three steps of the evolution of a single spin coupled to a harmonic oscillator mapped to two qubits, while in Figure 3b, we show our implementation of three-step evolution of the case with two spins and one harmonic oscillator. For considerations of connectivity, the auxiliary qubits needed for the dissipative channel are placed at the edges of the circuit, next to the spins. After all time-steps are finished, the qubits representing the spin(s) s_k and the bosons b_k are measured, while the state of the auxiliary qubit is ignored.

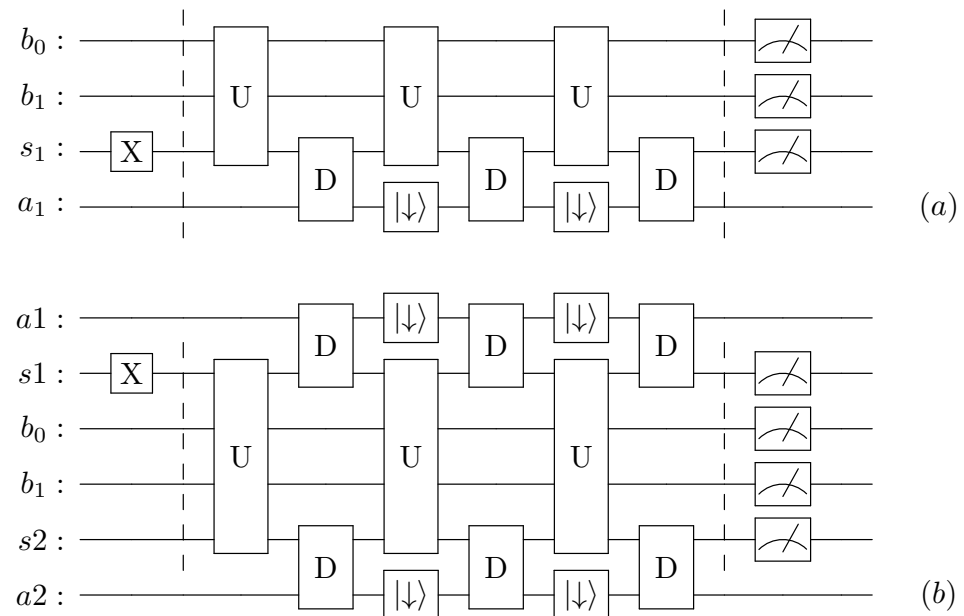


Figure 3. Circuit structure, alternating between a unitary evolution and collisions with auxiliary qubits and resets. (a) For a single spin and (b) two spin system. Here, the spins are represented by s_k , the harmonic oscillator modes (4 levels) are encoded in the b_k qubits and the auxiliary qubits are represented by a_k . X-Gate represents the initial state preparation, $|\downarrow\rangle$ represents resets, the final gates represent measurements, while D is described in Figure 2.

2.3. Quantum Hardware Simulation

To perform our quantum circuit simulations and run it on actual quantum hardware, we use IBM’s Qiskit software [65]. The Quantum Computer we use is the 7-qubit

ibmq_jakarta device with a native gate set {CNOT, ID, RZ, SX, X}. Each circuit is run with $2^{13} = 8192$ shots (repetitions).

We quantify the error at each point in time as the infidelity \mathcal{I} [67]

$$\mathcal{I}(\hat{\rho}, \hat{\rho}') = 1 - \left(\text{Tr} \left[\sqrt{\sqrt{\hat{\rho}} \hat{\rho}' \sqrt{\hat{\rho}}} \right] \right)^2 \tag{5}$$

where we obtain the density matrix $\hat{\rho}'$ of the circuit via quantum state tomography. We also consider a time-averaged version of the infidelity $\bar{\mathcal{I}}$, which is obtained by averaging the infidelity over time, except for the time $t = 0$, which consists of just the state preparation. The exact density matrix $\hat{\rho}$ for the benchmark is obtained from the exact evolution of the master Equation (Equation (2)), for which we use QuTiP [68]. To mitigate the measurement error on noisy hardware, we classically post-process the results with Qiskit’s error mitigation, which approximates the inverse of the noise matrix of the readout [69].

Reduced-Noise Models

While it is important to study how current quantum processors can evaluate the model we study, we also aim to explore what could be the performance of future, less noisy, hardware. To model these scenarios, we use the same error channels that IBM uses to describe their current devices.

The noise models include error sources in the gates, as thermal relaxation (relaxation and dephasing) and depolarizing errors, and also readout errors [70].

For our reduced-noise models we scale down the average gate infidelity \mathcal{I}_{Gate} , the gate times t_{Gate} , and the false-readout probabilities, probability of measuring 1 when the state is 0 $P(1|0)$ or vice versa $P(0|1)$, by the same noise-factor ζ , or more precisely

$$\mathcal{I}_{Gate} \rightarrow \zeta \cdot \mathcal{I}_{Gate} \tag{6}$$

$$t_{Gate} \rightarrow \zeta \cdot t_{Gate} \tag{7}$$

$$P(1|0), P(0|1) \rightarrow \zeta \cdot P(1|0), \zeta \cdot P(0|1) \tag{8}$$

where ζ ranges from 0 to 1.

Indeed, realistically some of these parameters will not see equal improvement in the coming years, but a more detailed analysis of differentiated improvements of different aspects is beyond the scope of this work. Details on the error channels can be found in Appendix B.

3. Results

Inaccuracies in the implementation of the model on a quantum computer can stem from different causes of completely different nature. We will first consider errors that rise from the Trotterization of the evolution in Section 3.1. We will then consider errors due to the noisy nature of the quantum computer in Section 3.2. In Section 3.3, we will then study the case of two spins coupled to the harmonic oscillator.

In the following, for the Hamiltonian, we choose the parameters $\epsilon = 0.5, \omega = 4, \lambda = 2$ for one spin and $\epsilon = 0.5, \omega = 6, \lambda = 2$ for two spins. For the open dissipative rate, we choose $\gamma = 1$. With these parameters, an accurate evolution of the system up to a time $t = 2$ can be obtained considering simply four levels for the harmonic oscillator, which can then be encoded with two qubits. For the initial state, we consider a pure product state between spins and bosons, with one spin in the excited state and zero excitations in the harmonic oscillator. This choice of initial conditions allows observing oscillatory, non-trivial dynamics from early times, while not requiring too many levels for the harmonic oscillator.

3.1. Error from the Circuit Implementation

As explained earlier, to implement the open dynamics, we Trotterize the unitary and dissipative parts of the master equation. However, for the implementation of the

unitary evolution, we need to rely on another layer of Trotterization. In Figure 4, we consider a unitary evolution with Hamiltonian \hat{H}_{SB} from Equation (1) for a time-step Δt and the possible implementation error, but considering no noise from the machine (blue lines). Implementing the various non-commuting terms of \hat{H}_{SB} in Qiskit [65] requires 48 single-qubit- and 19 CX-Gates or 79 single-qubit- and 28 CX-Gates, when using first or second-order Trotter, respectively, (Table A1).

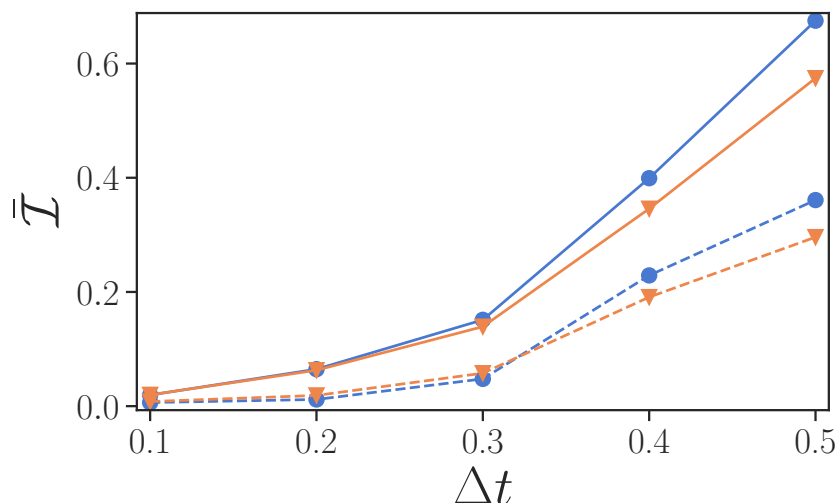


Figure 4. Time-averaged infidelity for the evolution from $t = 0$ to $t = 2$. Noiseless simulations of the Hamiltonian $\gamma = 0$ (blue line, dots) and the open system $\gamma = 1$ (orange line, triangle). The solid and dashed lines are used, respectively, for first-order and second-order Trotter implementations. The common parameters are $\epsilon = 0.5$, $\omega = 4$, $\lambda = 2$. The number of time-steps for $\Delta t = t/N$, $N = 0.1, 0.2, 0.3, 0.4, 0.5$ are $N = 20, 10, 7, 5, 4$, respectively, not counting $t = 0$, which just consists of the initial state preparation.

In Figure 4, we evaluate the infidelity for both unitary and dissipative evolutions, i.e., following Equation (2) for $\gamma = 0$ (blue lines with circles) or $\gamma = 1$ (orange lines with triangles), versus Δt . We observe that the second-order Trotterization, dashed lines, has significantly smaller infidelity than a first-order implementation, continuous lines. Interestingly, beyond $\Delta t \approx 0.3$, the infidelity in just the Hamiltonian simulation is larger than the infidelity when including the dissipation. Furthermore, independently of whether one considers first-order or second-order Trotterization, the dissipative dynamics has either smaller infidelity or it is very close to the unitary case. This implies that the unitary step implementing the Hamiltonian is the main contribution to the infidelity compared to the implementation of the dissipation.

3.2. Error in the Presence of Noise

We now turn to more realistic, and thus noisy, devices. In Figure 4, for noiseless simulations, we observed that the infidelity increases monotonously with the time-step size Δt , and that a second-order Trotterization is always preferred. In the presence of noise, however, an increased number of gates can lead to stronger noise effects, and thus instead of improving the quality of the simulations, it may result in worse fidelity. In Figure 5a, we thus consider the evolution of the full model, unitary and dissipative part, up to a time $t = 2$ for different magnitudes of noise $\zeta = 0.01, 0.1, 1$ (from lighter to darker colors), for either a first-order Trotter step (continuous lines) or a second-order Trotter step (dashed lines). In particular, we depict the infidelity versus the length of the time-step Δt . We observe that for intermediate values of noise $\zeta = 0.1, 1$ there is an optimal time interval Δt that corresponds to the lowest infidelity, and that first-order Trotterization can perform better at smaller Δt .

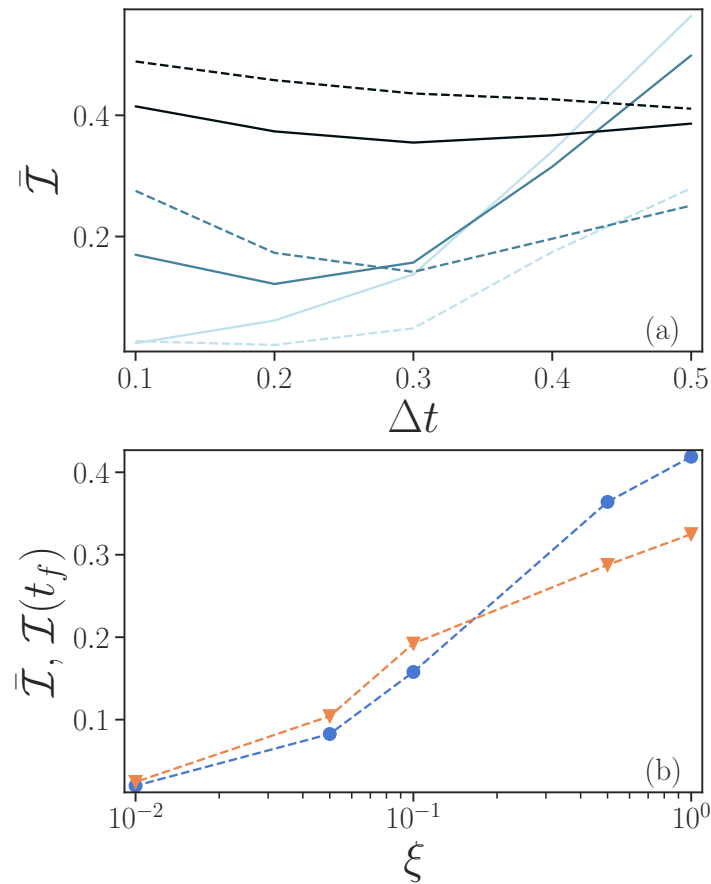


Figure 5. (a) Infidelity averaged over time as a function of time-step size Δt for an evolution from $t = 0$ to a final time $t_f = 2$. Different noise levels $\zeta = 0.01, 0.1, 1$ are represented by lighter to darker colors. (b) Time-averaged (blue circles) and final (orange triangles) infidelity as a function of noise levels. Here, the final time is taken as $t_f = 2$ and we choose $\Delta t = 0.2$. In both panels, results from first-order Trotter implementations are represented by continuous lines, while those from second-order are represented by dashed lines. Parameters $\epsilon = 0.5, \omega = 4, \lambda = 2, \gamma = 1$.

We now consider the open-system dynamics case. The impact of noise on fidelity is depicted in Figure 5b. Here, we show both the average infidelity over the time interval from $t = 0$ to $t = 2$ (blue line with circles), and the infidelity at the final time (orange line with triangles). We consider exclusively a second-order Trotter decomposition and a time-step $\Delta t = 0.2$. Figure 5b indicates a monotonous growth of infidelity with the noise-factor ζ , for the parameters explored.

In Figure 6, we show the infidelity versus time for first-order (solid lines) and second-order (dashed line) Trotterizations, while $\Delta t = 0.2$. We observe that, only for small values of ζ , one would prefer a second-order Trotterization to improve on the fidelity of the states. We note, not shown here, that for $\zeta = 0.01$, the dynamics is almost identical to the noiseless case.

To better understand the role of dissipation, we aim to verify its effect on the accuracy of the simulation. To focus specifically on the role of γ , we consider only a second-order Trotter evolution, a fixed value of $\Delta t = 0.2$ and $\zeta = 0.01$, where the simulation of the quantum computer shows generally better performance compared to levels of higher magnitudes of noise $\zeta = 0.1, 1$. In Figure 7a, we plot the time-averaged infidelity at different values of γ , with (an orange line with circles) and without noise (blue line with triangles). In noiseless simulations, the infidelity increases with γ , while in noisy simulations the infidelity initially reduces to a minimum at $\gamma = 1$. Our understanding is that the dissipation in the exact calculations acts in a similar way as the intrinsic noise on the device, by drawing the system to its ground state and reducing coherence. It can thus be easier

for a lossy quantum hardware to simulate a lossy system compared to a closed system ($\gamma = 0$). However, a system with larger γ also implies further difficulties in the simulations stemming, for example, from Trotterization. It thus occurs that the intrinsic dissipative dynamics can, in some regimes, be better represented on a noisy device.

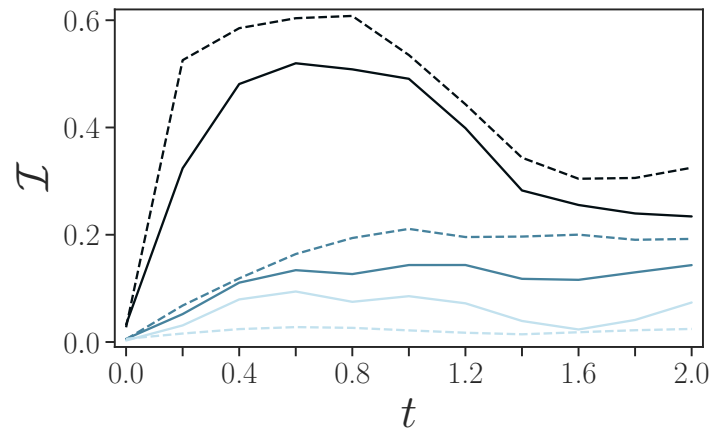


Figure 6. Infidelity as a function of time in open-system simulation in presence of noise. Using first-order Trotter (solid) and second-order Trotter (dashed) at $\Delta t = 0.2$. At noise-factor $\xi = 0.01, 0.1, 1$ (from lighter to darker colors). Other parameters are $\epsilon = 0.5, \omega = 4, \lambda = 2, \gamma = 1$.

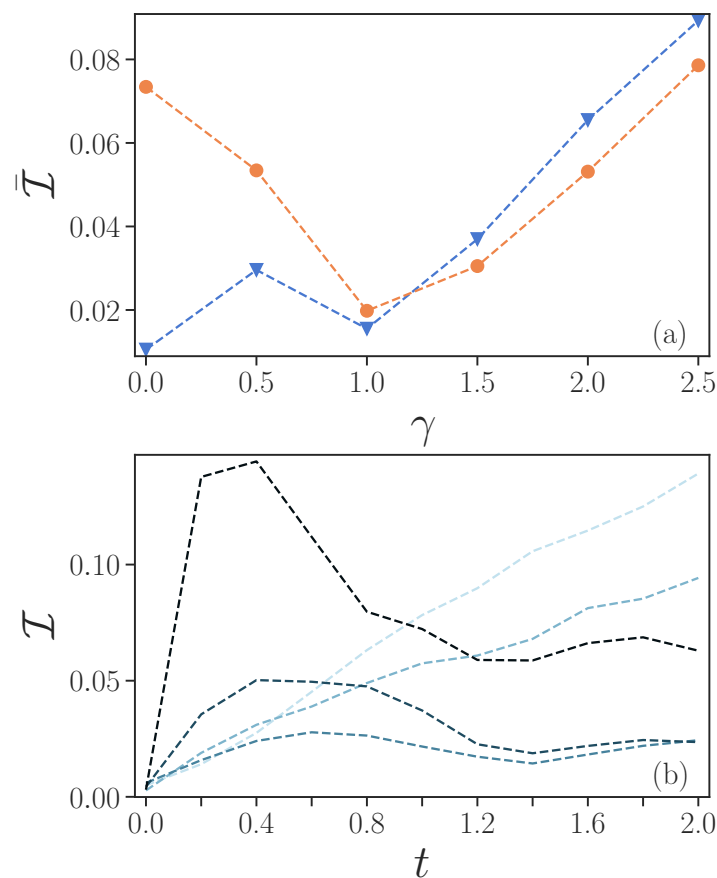


Figure 7. (a) Infidelity averaged over time versus dissipative rate γ with noise $\xi = 0.01$ (orange line with circles) and without noise (blue line with triangles). (b) Infidelity as a function of time $\gamma = 0, 0.5, 1, 1.5, 2, 2.5$ (from lighter to darker colors). Second-order Trotter at $\Delta t = 0.2$ and the other parameters are $\epsilon = 0.5, \omega = 4, \lambda = 2$.

In Figure 7b, we plot the infidelity versus time for different values of the dissipative rate γ . We observe that, for $\gamma \leq 1$, the infidelity tends to increase with time, while for larger values of $\gamma \geq 1.5$, the infidelity can decrease after a maximum at an earlier time $t \approx 0.4$.

Figure 8 shows the average occupation in the harmonic oscillator, panel (a), and the expectation values of $\hat{\sigma}^z$ of the spin, panel (b), versus time. In both panels, the dotted line corresponds to the exact values, whilst the solid and dashed lines to $\zeta = 0.01, 0.1, 1$, respectively, from lighter to darker shades, and solid lines are used for first-order Trotterizations, while dashed lines are used for second-order. For each noise level ζ , we used the Trotterization order which corresponds to the lower fidelity.

The oscillatory evolution of the occupation of the harmonic oscillator is captured, only partially, with the smaller non-zero noise parameter considered $\zeta = 0.01$, panel (a), while the occupation of the harmonic oscillator at $\zeta = 1$ quickly stagnates around a value of 1. Instead, the simpler evolution of $\hat{\sigma}^z$ is also captured fairly well for the different values of ζ , as the simulated dissipation of the spin is closer to the relaxation of the spin-qubit under noise.

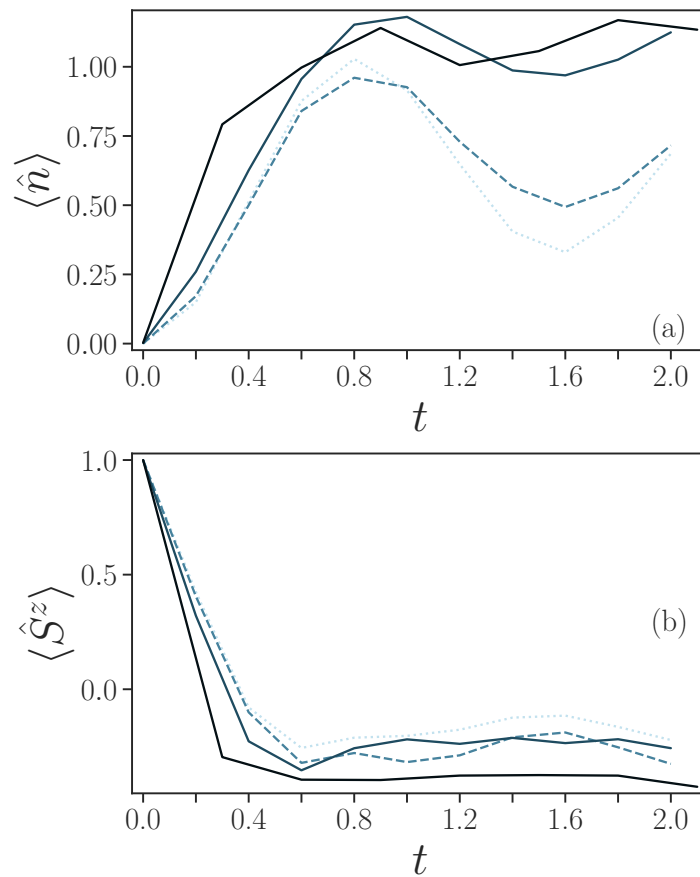


Figure 8. (a) Average bosonic occupation $\langle \hat{n} \rangle$ and (b) $\langle \hat{\sigma}^z \rangle$ as a function of time. Different noise levels $\zeta = 0.01, 0.1, 1$ are presented, respectively, by lighter to darker colors. As a reference, exact simulations are depicted by dotted lines. Results obtained using first-order Trotterization are with solid lines, while second-order with dashed lines. Other parameters are $\epsilon = 0.5, \omega = 4, \lambda = 2$ and $\gamma = 1$.

3.3. Two-Spin System

We here extend the system to two spins to see whether it is possible to the study correlation developing between them through a mediated interaction via the harmonic oscillator, as the two spins do not directly interact with each other. We use the parameters $\epsilon = 0.5, \omega = 6, \lambda = 2$ and $\gamma = 1$. We prepare the initial state in a product state of one spin in the excited state, one in the ground state, and the harmonic oscillator as completely empty. This allows us to observe non-trivial dynamics while still requiring just a few occupied levels of the harmonic oscillator.

As for the single-spin simulations, we first evaluate infidelity in the presence of noise. Simulating two spins requires roughly twice the number of gates as simulating one spin. A single Δt evolution with a first-order Trotter requires 113 single-qubits and 36 CX-Gates, while the second-order Trotter requires 177 single-qubits and 70 CX gates, as can be seen in Figure A1 and Table A1 in Appendix A. Furthermore, in the case of two spins, we find the optimal Trotter time-step Δt to be the same as for the single spin case (not shown).

To study the emerging correlations between the spins mediated by interaction with the photons, we consider the spin–spin correlators

$$\begin{aligned} C^{ZZ} &= \langle \hat{\sigma}_1^z \hat{\sigma}_2^z \rangle - \langle \hat{\sigma}_1^z \rangle \langle \hat{\sigma}_2^z \rangle \\ C^{XX} &= \langle \hat{\sigma}_1^x \hat{\sigma}_2^x \rangle - \langle \hat{\sigma}_1^x \rangle \langle \hat{\sigma}_2^x \rangle. \end{aligned} \tag{9}$$

These connected correlation functions (also called second-order Ursell functions or cumulants) correspond to the covariance in statistics and vanish if and only if $\hat{\sigma}_1^{(\cdot)}$ and $\hat{\sigma}_2^{(\cdot)}$ are statistically independent [71–73].

In Figure 9, we show C^{ZZ} and C^{XX} for, again, $\zeta = 0.01, 0.1, 1$ from lighter to darker lines. The solid lines correspond to first-order Trotter and dashed lines to second-order Trotter and these Trotterization orders have been chosen as they result, for the respective amount of noise, in the lowest infidelity. In both panels, the dotted lines correspond to the exact values. The exact case simulations show a build-up in anti-correlation in z direction at $t = 0.4$, before reducing to 0 which can already be observed for $\zeta = 0.1$. A correlation in x direction builds up monotonously over time and one would need $\zeta = 0.01$ for a clearer signal.

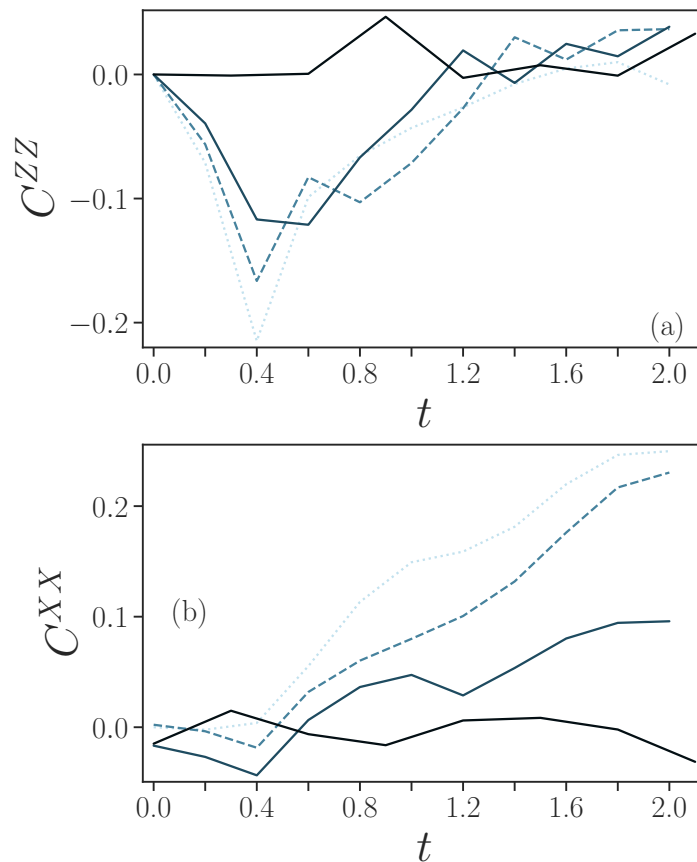


Figure 9. Correlations for the case of two spins: (a) spin-z connected correlation C^{ZZ} (b) spin-x connected correlation C^{XX} as a function of time. Different noise levels $\zeta = 0.01, 0.1, 1$ are presented, respectively, by lighter and darker colors. As a reference, exact simulations are depicted by the dotted lines. Results obtained using first-order Trotterization are represented by solid lines, while those using second-order Trotterization are represented by dashed lines. Other parameters are $\epsilon = 0.5$, $\omega = 6$, $\lambda = 2$ and $\gamma = 1$.

In principle, correlations could be observed for a higher number of spins. In practice, the larger number of qubits needed, and their connectivity, would result in an increased number of gates which would limit the fidelity in NISQ devices. We also note that, going from one to two spins, we had to increase ω to keep the higher levels of the harmonic oscillator sparsely populated. If one does not want to increase the number of levels studied for the harmonic oscillator, a similar adjustment, such as decreasing the coupling between the harmonic oscillator and the spins, would be necessary when increasing the number of spins.

4. Conclusions

In this paper, we have studied the feasibility of simulating open spin-boson dynamics on a quantum computer. We used a second-quantization mapping of the bosonic degrees of freedom and Trotterization of the unitary to implement the Hamiltonian. To implement the dissipative dynamics, we used collisions and resets with auxiliary qubits.

We found that, in our parameter regime, the Hamiltonian simulation is the limiting factor to the fidelity. We surveyed optimal Trotterization formulas and time-step sizes depending on the level of noise in the system. We selected the open dissipative rate with the highest fidelity in noisy circuits, and we found that current noise levels in the machine we considered would make such simulations particularly challenging.

Anticipating future improved devices, we ran our simulations on 10% and 1% of current noise levels, and we were able to show that it would be possible to attain much higher fidelities. Furthermore, certain observables could be well represented with larger amounts of noise. Importantly, the simulation of an open system can be more accurate than unitary evolution as the open system dynamics could be closer to how a noisy computer is already affecting a state.

Future developments in noise reduction in the hardware, in post-processing error mitigation, as well as in reducing the number of gates for unitary evolutions can lead to a significant increase in simulation power.

In our system, we have limited the dissipation to the spins. An interesting avenue for future work could be the inclusion of loss in the bosonic degrees of freedom of the cavity, for which additional auxiliary qubits, gates, and connectivity requirements could prove challenging.

Author Contributions: Conceptualization, L.C.K. and D.P.; methodology, D.P.; software, A.B.; validation, A.B., L.C.K. and D.P.; formal analysis, A.B.; investigation, A.B.; resources, L.C.K.; data curation, A.B.; writing—original draft preparation, A.B.; writing—review and editing, D.P.; visualization, A.B.; supervision, D.P.; project administration, L.C.K.; funding acquisition, D.P. All authors have read and agreed to the published version of the manuscript.

Funding: This research received no external funding.

Data Availability Statement: The data presented in this study are available on request from the corresponding author.

Acknowledgments: A.B. acknowledges support from the Ministry of Education of Singapore AcRF MOE Tier-II (Project No. T2MOE2002). L.C.K. and D.P. acknowledge support from the National Research Foundation, Singapore under its QEP2.0 program (NRF2021-QEP2-02-P03).

Conflicts of Interest: The authors declare no conflict of interest.

Appendix A. Encoding of Bosonic Operators Onto Qubits

We will quickly review the d-level-to-qubit mapping we used to encode the bosonic operators as strings of Pauli matrices. The method and different binary encodings are discussed in [31]. The steps can be summarized as:

1. Truncate the infinite-dimensional harmonic oscillator at some level d_{HO}
2. Rewrite each bosonic operator \hat{A} as a sum of level transitions

$$\hat{A} = \sum_{l,l'=0}^{d_{HO}-1} a_{l,l'} |l\rangle \langle l'|, \hat{A} = \{\hat{a}, \hat{a}^\dagger, \hat{a}^\dagger \hat{a}\}$$

3. Assign each level an integer

$$|l\rangle \xrightarrow{\text{integer}} |i\rangle, i \in \mathbb{N}$$

4. Write each integer in binary

$$|i\rangle \xrightarrow{\text{integer-to-bit}} \bigotimes_{m=1}^{Q_B} |b_m\rangle, b_m \in \{0,1\}$$

5. Map each bit pair $|b_m\rangle \langle b'_m|$ to Pauli matrices using

$$\begin{aligned} |0\rangle \langle 0| &= \frac{1}{2}(\mathbb{1} + \hat{\sigma}^z) \\ |1\rangle \langle 1| &= \frac{1}{2}(\mathbb{1} - \hat{\sigma}^z) \\ |0\rangle \langle 1| &= \frac{1}{2}(\hat{\sigma}^x + i\hat{\sigma}^y) = \hat{\sigma}^+ \\ |1\rangle \langle 0| &= \frac{1}{2}(\hat{\sigma}^x - i\hat{\sigma}^y) = \hat{\sigma}^- \end{aligned}$$

The result is that each level transition is written as a string of Pauli operators and each bosonic operator \hat{A} as a sum of N_P Pauli strings

$$\hat{A} = \sum_{k=1}^{N_P} c_k \bigotimes_{j=1}^{Q_B} \hat{\sigma}_{kj}, \hat{\sigma}_{kj} \in \{\mathbb{1}, \hat{\sigma}^x, \hat{\sigma}^y, \hat{\sigma}^z\} \tag{A1}$$

where $Q_B = \lceil \sqrt{d_{HO}} \rceil$ is the number of qubits which encode the bosonic levels ($\lceil \cdot \rceil$ is the ceiling function).

Appendix A.1. Gate Requirements

When writing the integers in binary in step 4, different integer-to-bit encodings result in different Pauli strings and ultimately in a different representation of the Hamiltonian. While the representations of the Hamiltonian are theoretically equivalent, they come with different gate counts and thus result in different performances on noise devices.

As integer-to-bit encodings, we considered standard binary and gray code, since both of these are compact, i.e., they require the minimum amount of qubits. Table A1 shows the gates required to evolve one time-step of the Trotterized unitary $e^{-i\hat{H}_{SB}\Delta t}$ and dissipation on the ibmq_jakarta device. This includes additional CX-Gates to implement any necessary SWAP-Gates due to limited qubit connectivity (Figure A1). For our Hamiltonian \hat{H}_{SB} , gray code yielded less gates than standard binary in all cases, which is why we used gray code throughout the main text.

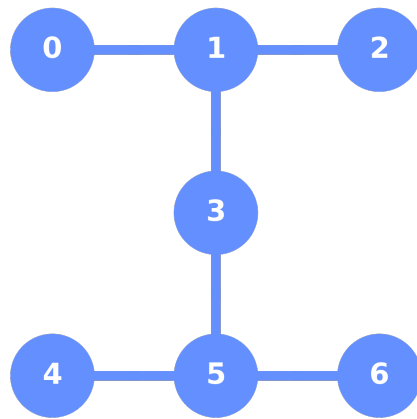


Figure A1. Qubit connectivity of the used ibmq_jakarta device.

Table A1. Gate counts, both for CX-Gate and single-qubit gates, to evolve one time-step of master Equation (2) on the Jakarta device.

N_S	d_{HO}	Trotter order	Standard Binary		Gray Code	
			Single	CX	Single	CX
1	4	First	53	21	94	43
1	4	Second	94	34	75	28
1	8	First	156	66	122	60
1	8	Second	282	124	191	107
2	4	First	106	37	122	36
2	4	Second	191	65	168	74
2	8	First	270	139	200	156
2	8	Second	496	272	409	255

Appendix A.2. Mapped Hamiltonian

After the mapping of the harmonic oscillator to qubits, the Hamiltonian (Equation (1)) is written as a sum of Pauli strings h_k . The unitary $e^{\sum_k h_k}$ is then Trotterized (Equation (3)). The mapped Hamiltonian $\hat{H}_{SB} = \sum_k h_k$ we implemented for the main text reads explicitly

$$\begin{aligned} \hat{H}_{SB} = & -\sqrt{2}\sigma^x_0\sigma^x_1\sigma^z_2 + \sqrt{2}\sigma^x_0\sigma^x_1 \\ & + (1 - \sqrt{3})\sigma^x_0\sigma^x_2\sigma^z_1 + (1 + \sqrt{3})\sigma^x_0\sigma^x_2 \\ & + \frac{1}{4}\sigma^x_0 - \frac{1}{2}\sigma^z_0 - 2\sigma^z_1\sigma^z_2 - 4\sigma^z_1 \end{aligned} \tag{A2}$$

for the single spin case, and

$$\begin{aligned} \hat{H}_{SB} = & -\sqrt{2}\sigma^x_0\sigma^x_1\sigma^z_2 + \sqrt{2}\sigma^x_0\sigma^x_1 \\ & + (1 - \sqrt{3})\sigma^x_0\sigma^x_2\sigma^z_1 + (1 + \sqrt{3})\sigma^x_0\sigma^x_2 \\ & + \frac{1}{4}\sigma^x_0 - \sqrt{2}\sigma^x_1\sigma^x_3\sigma^z_2 + \sqrt{2}\sigma^x_1\sigma^x_3 \\ & + (1 - \sqrt{3})\sigma^x_2\sigma^x_3\sigma^z_1 + (1 + \sqrt{3})\sigma^x_2\sigma^x_3 \\ & + \frac{1}{4}\sigma^x_3 - \frac{1}{2}\sigma^z_0 - 3\sigma^z_1\sigma^z_2 - 6\sigma^z_1 \\ & - \frac{1}{2}\sigma^z_3 \end{aligned} \tag{A3}$$

for two spins case. Each term constitutes one of the h_k in Equations (3) and (4).

Appendix B. Noise Model

Qiskit supplies noise models based on device properties measured during calibration. In order to simulate an improved future device, we engineer our noise from an identical model, but from lower noise levels.

The noise model contains three error sources [70]: (i) thermal relaxation (relaxation and dephasing); (ii) depolarizing (Pauli) error; and (iii) readout (measurement) error. At every gate, first the thermal relaxation and then the depolarizing error is applied. The strength of the depolarizing error is calculated backwards, to reach a target ‘gate error’ when combined with the thermal relaxation. Details can be found at [74].

Appendix B.1. Error Sources

Appendix B.1.1. Thermal Relaxation Error

Thermal relaxation is defined by the qubit-specific parameters T_1 time, T_2 time, qubit frequency f_{Qubit} and qubit temperature \mathcal{T}_{Qubit} . The thermal error channel is then given time to act according to a gate-dependent gate time. For two-qubit-gates, the error is simply the tensor product between two single-qubit channels.

T_1 is qubit-specific time until relaxation, i.e., to decay from the excited state to the ground state. T_2 qubit-specific coherence time, or time until dephasing. The qubit frequency f_{Qubit} is the difference in energy between the ground and excited states. The qubit temperature \mathcal{T}_{Qubit} is assumed to be 0 in Qiskit’s and our noise models.

The qubit frequency and temperature enter only via the excited state population. If $f_{Qubit} \rightarrow \infty$ or $\mathcal{T}_{Qubit} = 0$, the excited state population is 0. Since $\mathcal{T}_{Qubit} = 0$ in our models, both the frequency and temperature can effectively be ignored as parameters.

For $T_2 < T_1$, thermal relaxation is most straightforwardly described by (assuming the device to be at 0 temperature)

$$K_{T_0} = \sqrt{\mathcal{P}_1} \mathbb{1}, \tag{A4}$$

$$K_{T_1} = \sqrt{\mathcal{P}_Z} \hat{\sigma}^z, K_{T_2} = \sqrt{\mathcal{P}_{reset}} |\downarrow\rangle \langle \downarrow| \tag{A5}$$

$$\mathcal{E}_T(\hat{\rho}) = \sum_{i=10}^2 K_{T_k} \hat{\rho} K_{T_k}^\dagger \tag{A6}$$

It is composed of the probabilities of a phase-flip \mathcal{P}_Z , a reset to the ground state \mathcal{P}_{reset} , or for nothing to happen \mathcal{P}_1 . The probabilities $\mathcal{P}_Z, \mathcal{P}_{reset}$ are calculated from T_1, T_2 and the gate time t_{Gate} .

$$\mathcal{P}_{reset} = 1 - \mathcal{P}_{T_1} = 1 - e^{-t_{Gate} \cdot \frac{1}{T_1}} \tag{A7}$$

$$\mathcal{P}_Z = (1 - \mathcal{P}_{reset}) \left(1 - \frac{\mathcal{P}_{T_2}}{\mathcal{P}_{T_1}} \right) / 2 \tag{A8}$$

$$= (1 - \mathcal{P}_{reset}) \left(1 - e^{-t_{Gate} \cdot \left(\frac{1}{T_2} - \frac{1}{T_1} \right)} \right) / 2 \tag{A9}$$

$$\mathcal{P}_1 = 1 - \mathcal{P}_Z - \mathcal{P}_{reset}. \tag{A10}$$

If $2T_1 \geq T_2 > T_1$ thermal relaxation has to be described by its Choi matrix

$$\hat{\rho} \rightarrow \mathcal{E}_T(\hat{\rho}) = tr_1[C(\hat{\rho}^T \otimes I)] \tag{A11}$$

$$C_{\mathcal{E}_T} = \begin{pmatrix} 1 & 0 & 0 & \mathcal{P}_{T_2} \\ 0 & 0 & 0 & 0 \\ 0 & 0 & \mathcal{P}_{reset} & 0 \\ \mathcal{P}_{T_2} & 0 & 0 & 1 - \mathcal{P}_{reset} \end{pmatrix} \tag{A12}$$

which can also be used if $T_2 < T_1$ to compute the process fidelity in Equation (A21).

At the time of writing, all qubits on the Jakarta hardware satisfied $T_2 < T_1$. This is not necessarily the case for all devices provided by IBM or in general.

Appendix B.1.2. Depolarizing Error

The depolarizing noise (or Pauli) channel is composed of either a bit-flip ($\hat{\sigma}^x$), a phase-flip ($\hat{\sigma}^z$) or both at the same time ($\hat{\sigma}^y$), all with equal probability [70].

$$\hat{\rho} \rightarrow \mathcal{E}_D(\hat{\rho}) = \sum_{i=1}^3 K_{\mathcal{P}_i} \hat{\rho} K_{\mathcal{P}_i}^\dagger \tag{A13}$$

$$K_{\mathcal{P}_0} = \sqrt{1 - \mathcal{P}_D} \mathbb{1}, K_{\mathcal{P}_1} = \sqrt{\frac{\mathcal{P}_D}{3}} \hat{\sigma}^x \tag{A14}$$

$$K_{\mathcal{P}_2} = \sqrt{\frac{\mathcal{P}_D}{3}} \hat{\sigma}^y, K_{\mathcal{P}_3} = \sqrt{\frac{\mathcal{P}_D}{3}} \hat{\sigma}^z \tag{A15}$$

Gate Infidelity

The probability of a depolarizing error is calculated from the target gate infidelity \mathcal{I}_{Gate} , and the infidelity due to thermal relaxation \mathcal{I}_T .

$$\mathcal{I}_D = \mathcal{I}_{Gate} - \mathcal{I}_T \tag{A16}$$

The target gate infidelity is given as a parameter, while \mathcal{I}_T has to be calculated as

$$\mathcal{F}_T = 1 - \mathcal{I}_T \tag{A17}$$

$$= \mathcal{F}_{avg}(\mathcal{E}_T, U) \tag{A18}$$

$$= \int d\psi \langle \psi | U^\dagger \mathcal{E}_T(|\psi\rangle\langle\psi|) U | \psi \rangle \tag{A19}$$

$$= \frac{d\mathcal{I}_{pro}(\mathcal{E}_T, U) + 1}{d + 1} \tag{A20}$$

where $\mathcal{I}_{pro}(\mathcal{E}_T, U)$ is the process fidelity of the input quantum channel \mathcal{E}_T with a target unitary U , and d is the dimension of the channel.

$$\mathcal{I}_{pro}(\mathcal{E}_T, \mathcal{F}) = F(C_{\mathcal{E}_T}/d, \rho_{\mathcal{F}}) \tag{A21}$$

where \mathcal{F} is the state fidelity as defined in the main text

$$\mathcal{F}(\rho_1, \rho_2) = \left(\text{Tr} \left[\sqrt{\sqrt{\rho_1} \rho_2 \sqrt{\rho_1}} \right] \right)^2 \tag{A22}$$

$C_{\mathcal{E}_T}/d$ is the normalized Choi matrix for the channel \mathcal{E}_T , and d is the input dimension of \mathcal{E}_T .

Importantly, for our reduced-noise models, the infidelity from thermal relaxation \mathcal{I}_T is linear in the gate time t_{Gate} . Thus, when we rescale $\mathcal{I}_{Gate} \rightarrow \xi \cdot \mathcal{I}_{Gate}$, $t_{Gate} \rightarrow \xi \cdot t_{Gate}$, we indirectly scale $\mathcal{I}_D \rightarrow \xi \cdot \mathcal{I}_D$, $\mathcal{I}_T \rightarrow \xi \cdot \mathcal{I}_T$. This way, the relative contribution of the error channels $\mathcal{I}_D/\mathcal{I}_T$ to the infidelity remains unchanged.

Depolarizing Error Probability

If we write the depolarizing error in terms of the identity and the complete depolarizing channel D , we can rewrite the gate fidelity

$$\mathcal{E}_D = (1 - \mathcal{P}_D) \cdot \mathbb{1} + \mathcal{P}_D \cdot D \tag{A23}$$

$$\mathcal{F}_{gate} = 1 - \mathcal{I}_{Gate} \tag{A24}$$

$$= \mathcal{F}(\mathcal{E}_D \cdot \mathcal{E}_T) \tag{A25}$$

$$= (1 - \mathcal{P}_D)\mathcal{F}_T + \mathcal{P}_D \cdot \mathcal{F}_D \tag{A26}$$

$$= \mathcal{F}_T - \mathcal{P}_D \cdot (d \cdot \mathcal{F}_T - 1)/d \tag{A27}$$

where $d = 2^{qubits}$ is the dimensionality of the gate. From this, the solution to the depolarizing error probability is

$$\mathcal{P}_D = d(\mathcal{F}_T - \mathcal{F}_{gate}) / (d \cdot \mathcal{F}_T - 1) \tag{A28}$$

$$= d(\mathcal{I}_{Gate} - \mathcal{I}_T) / (d \cdot \mathcal{F}_T - 1) \tag{A29}$$

More details can be found at [74].

Appendix B.1.3. Measurement Error

A measurement error is equivalent to a bit-flip $\hat{\sigma}^x$ followed by a noiseless readout [70]. The probability of the readout error \mathcal{P}_R is given by the probability $P(n|m)$ of recording a noisy measurement outcome as n , given that the true measurement outcome is m .

$$K_{R_0} = \sqrt{1 - \mathcal{P}_R}\mathbb{1}, K_{R_1} = \sqrt{\mathcal{P}_R}\hat{\sigma}^x \tag{A30}$$

$$\mathcal{P}_R = \sum_{n \neq m} P(n|m) \tag{A31}$$

where n, m run over all qubits, in the case of two qubits $n, m \in \{00, 01, 10, 11\}$. See [74] for further details.

Appendix B.1.4. Error Sources in the Reference Device

Given the three error sources, one can ask which error source causes the dominant contribution to the noise in our results. As we use measurement error mitigation and it is independent of the circuit depth, we will ignore the measurement error. Instead, we focus on the ratio of thermal and depolarizing errors in contributing to the infidelity, $\mathcal{I}_T/\mathcal{I}_D$. To give a rough estimation, we assume all gates $g \in \{CNOT, RZ, SX, X\}$ and all qubits q are used equally often, and average over both.

$$\mathcal{I}_T/\mathcal{I}_D = \frac{1}{N_q} \sum_{q=1}^{N_q=7} \left(\frac{1}{N_g} \sum_g^{N_g=4} \left(\frac{\mathcal{I}_T(q, g)}{\mathcal{I}_D(q, g)} \right) \right) \tag{A32}$$

We calculate $\mathcal{I}_T(q, g)$ and $\mathcal{I}_D(q, g)$ using Equations (A17) and (A16), respectively, and obtain the current calibration data from IBM. At the time of writing, the result for the Jakarta device is $\mathcal{I}_T/\mathcal{I}_D = 15.4$. We conclude that thermal relaxation is the main source of infidelity in our simulations, by one order of magnitude compared to depolarization.

Appendix B.1.5. Calibration Data

We base our reduced-noise models on the same hardware that we run our full-noise circuits on, the 7 qubit IBMQ Jakarta device.

At the time of writing, the calibration data are:

Processor: Falcon r5.11H, V1.1.0

Avg. CX-Gate error: $1.109e^{-2}$

Avg. readout error: $3.349e^{-2}$

Avg. T_1 : 139.01 us
 Avg. T_2 : 44.82 us
 Avg. gate time: 454.095 ns
 Avg. qubit frequency: 5.08 GHz
 Avg. qubit anharmonicity -0.329 GHz
 For more details, see [75].

Appendix C. Gate Definition

Some of the gates used are defined here. A controlled operation CO is defined as

$$CO(\theta) = I \otimes |\downarrow\rangle\langle\downarrow| + O(\theta) \otimes |\uparrow\rangle\langle\uparrow|, \tag{A33}$$

where the operation O is a X gate in case of the CX-Gate, or a rotation around the y-axis R_Y or z axis R_Z . R_Y and R_Z are, respectively, defined as

$$R_Y(\theta) = \exp\left(-i\frac{\theta}{2}Y\right) = \begin{pmatrix} \cos\frac{\theta}{2} & -\sin\frac{\theta}{2} \\ \sin\frac{\theta}{2} & \cos\frac{\theta}{2} \end{pmatrix}, \tag{A34}$$

$$R_Z(\lambda) = \exp\left(-i\frac{\lambda}{2}Z\right) = \begin{pmatrix} e^{-i\frac{\lambda}{2}} & 0 \\ 0 & e^{i\frac{\lambda}{2}} \end{pmatrix}. \tag{A35}$$

Furthermore, the \sqrt{X} gate is given by

$$\sqrt{X} = \frac{1}{2} \begin{pmatrix} 1+i & 1-i \\ 1-i & 1+i \end{pmatrix}. \tag{A36}$$

Appendix D. Transpiled Circuits

The amplitude damping circuit as in Figure 2 uses gates which are not available on the quantum computer we were using. Instead, the IBM Jakarta device uses the gate set {CNOT, ID, RZ, SX, X}. The amplitude damping circuit, in terms of these gates and as it was implemented on the hardware, is in Figure A2.

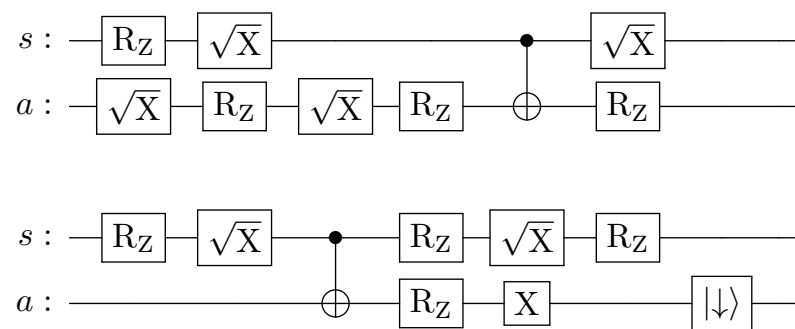


Figure A2. The dissipation circuit represented in Figure 2 in terms of the gates available on the IBM Jakarta device. Both lines for qubits s, a continue from the first row to the second.

References

- Lloyd, S. Universal Quantum Simulators. *Science* **1996**, *273*, 1073–1078. [CrossRef] [PubMed]
- Nielsen, M.A.; Chuang, I.L. *Quantum Computation and Quantum Information: 10th Anniversary Edition*; Cambridge University Press: Cambridge, UK, 2010. [CrossRef]
- Whitfield, J.D.; Biamonte, J.; Aspuru-Guzik, A. Simulation of Electronic Structure Hamiltonians Using Quantum Computers. *Mol. Phys.* **2011**, *109*, 735–750. [CrossRef]
- Wiebe, N.; Berry, D.W.; Høyer, P.; Sanders, B.C. Simulating quantum dynamics on a quantum computer. *J. Phys. A Math. Theor.* **2011**, *44*, 445308. [CrossRef]
- Tacchino, F.; Chiesa, A.; Carretta, S.; Gerace, D. Quantum Computers as Universal Quantum Simulators: State-of-the-Art and Perspectives. *Adv. Quantum Technol.* **2019**, *3*, 1900052. [CrossRef]

6. Jaderberg, B.; Eisfeld, A.; Jaksch, D.; Mostame, S. Recompilation-enhanced simulation of electron–phonon dynamics on IBM quantum computers. *New J. Phys.* **2022**, *24*, 093017. [[CrossRef](#)]
7. Leggett, A.J.; Chakravarty, S.; Dorsey, A.T.; Fisher, M.P.A.; Garg, A.; Zwerger, W. Dynamics of the dissipative two-state system. *Rev. Mod. Phys.* **1987**, *59*, 1–85. [[CrossRef](#)]
8. Weiss, U. *Quantum Dissipative Systems*; World Scientific: Singapore, 2011. [[CrossRef](#)]
9. Xu, D.; Schulten, K. Coupling of protein motion to electron transfer in a photosynthetic reaction center: Investigating the low temperature behavior in the framework of the spin–Boson model. *Chem. Phys.* **1994**, *182*, 91–117. [[CrossRef](#)]
10. Renger, T.; Marcus, R.A. On the relation of protein dynamics and exciton relaxation in pigment–protein complexes: An estimation of the spectral density and a theory for the calculation of optical spectra. *J. Chem. Phys.* **2002**, *116*, 9997–10019. [[CrossRef](#)]
11. Fleming, G.R.; Cho, M. Chromophore solvent dynamics. *Annu. Rev. Phys. Chem.* **1996**, *47*, 109–134. [[CrossRef](#)]
12. Preskill, J. Quantum Computing in the NISQ era and beyond. *Quantum* **2018**, *2*, 79. [[CrossRef](#)]
13. Bharti, K.; Cervera-Lierta, A.; Kyaw, T.H.; Haug, T.; Alperin-Lea, S.; Anand, A.; Degroote, M.; Heimonen, H.; Kottmann, J.S.; Menke, T.; et al. Noisy intermediate-scale quantum algorithms. *Rev. Mod. Phys.* **2022**, *94*, 015004. [[CrossRef](#)]
14. Peruzzo, A.; McClean, J.; Shadbolt, P.; Yung, M.H.; Zhou, X.Q.; Love, P.J.; Aspuru-Guzik, A.; O’Brien, J.L. A variational eigenvalue solver on a photonic quantum processor. *Nat. Commun.* **2014**, *5*, 4213. [[CrossRef](#)] [[PubMed](#)]
15. Farhi, E.; Goldstone, J.; Gutmann, S. A Quantum Approximate Optimization Algorithm. *arXiv* **2014**, arXiv:1411.4028. [[CrossRef](#)]
16. Erbanni, R.; Bharti, K.; Kwek, L.C.; Poletti, D. NISQ algorithm for the matrix elements of a generic observable. *arXiv* **2022**, arXiv:2205.10058. [[CrossRef](#)]
17. Li, Y.; Benjamin, S.C. Efficient Variational Quantum Simulator Incorporating Active Error Minimization. *Phys. Rev. X* **2017**, *7*, 021050. [[CrossRef](#)]
18. Temme, K.; Bravyi, S.; Gambetta, J.M. Error Mitigation for Short-Depth Quantum Circuits. *Phys. Rev. Lett.* **2017**, *119*, 180509. [[CrossRef](#)]
19. Endo, S.; Cai, Z.; Benjamin, S.C.; Yuan, X. Hybrid Quantum-Classical Algorithms and Quantum Error Mitigation. *J. Phys. Soc. Jpn.* **2021**, *90*, 032001. [[CrossRef](#)]
20. Di Paolo, A.; Barkoutsos, P.K.; Tavernelli, I.; Blais, A. Variational Quantum Simulation of Ultrastrong Light-Matter Coupling. *Phys. Rev. Res.* **2020**, *2*, 033364. [[CrossRef](#)]
21. Miessen, A.; Ollitrault, P.J.; Tavernelli, I. Quantum algorithms for quantum dynamics: A performance study on the spin-boson model. *Phys. Rev. Res.* **2021**, *3*, 043212. [[CrossRef](#)]
22. Fitzpatrick, N.; Apel, H.; Ramo, D.M. Evaluating low-depth quantum algorithms for time evolution on fermion-boson systems. *arXiv* **2021**, arXiv:2106.03985. [[CrossRef](#)]
23. Kamakari, H.; Sun, S.N.; Motta, M.; Minnich, A.J. Digital quantum simulation of open quantum systems using quantum imaginary time evolution. *PRX Quantum* **2022**, *3*, 010320. [[CrossRef](#)]
24. McArdle, S.; Jones, T.; Endo, S.; Li, Y.; Benjamin, S.C.; Yuan, X. Variational ansatz-based quantum simulation of imaginary time evolution. *Npj Quantum Inf.* **2019**, *5*, 75. [[CrossRef](#)]
25. Endo, S.; Sun, J.; Li, Y.; Benjamin, S.; Yuan, X. Variational quantum simulation of general processes. *Phys. Rev. Lett.* **2020**, *125*, 010501. [[CrossRef](#)] [[PubMed](#)]
26. Yoshioka, N.; Nakagawa, Y.O.; Mitarai, K.; Fujii, K. Variational quantum algorithm for nonequilibrium steady states. *Phys. Rev. Res.* **2020**, *2*, 043289. [[CrossRef](#)]
27. Liu, H.Y.; Sun, T.P.; Wu, Y.C.; Guo, G.P. Variational Quantum Algorithms for the Steady States of Open Quantum Systems. *Chin. Phys. Lett.* **2021**, *38*, 080301. [[CrossRef](#)]
28. Bharti, K.; Haug, T. Quantum-assisted simulator. *Phys. Rev. A* **2021**, *104*, 042418. [[CrossRef](#)]
29. Macridin, A.; Spentzouris, P.; Amundson, J.; Harnik, R. Digital quantum computation of fermion-boson interacting systems. *Phys. Rev. A* **2018**, *98*, 042312. [[CrossRef](#)]
30. Somma, R.D.; Ortiz, G.; Knill, E.H.; Gubernatis, J. Quantum simulations of physics problems. In Proceedings of the Quantum Information and Computation, SPIE, Orlando, FL, USA, 21–25 April 2003; Volume 5105, pp. 96–103. [[CrossRef](#)]
31. Sawaya, N.P.D.; Menke, T.; Kyaw, T.H.; Johri, S.; Aspuru-Guzik, A.; Guerreschi, G.G. Resource-efficient digital quantum simulation of d-level systems for photonic, vibrational, and spin-s Hamiltonians. *NPJ Quantum Inf.* **2020**, *6*, 49. [[CrossRef](#)]
32. Hu, Z.; Xia, R.; Kais, S. A quantum algorithm for evolving open quantum dynamics on quantum computing devices. *Sci. Rep.* **2020**, *10*, 3301. [[CrossRef](#)]
33. Schlimgen, A.W.; Head-Marsden, K.; Sager, L.M.; Narang, P.; Mazziotti, D.A. Quantum Simulation of Open Quantum Systems Using a Unitary Decomposition of Operators. *Phys. Rev. Lett.* **2021**, *127*, 270503. [[CrossRef](#)]
34. Udayakumar, P.; Kumar-Eslami, P. Kraus operator formalism for quantum multiplexer operations for arbitrary two-qubit mixed states. *Quantum Inf. Process.* **2019**, *18*, 361. [[CrossRef](#)]
35. García-Pérez, G.; Rossi, M.A.C.; Maniscalco, S. IBM Q Experience as a versatile experimental testbed for simulating open quantum systems. *Npj Quantum Inf.* **2020**, *6*, 1–10. [[CrossRef](#)]
36. Wei, S.J.; Ruan, D.; Long, G.L. Duality quantum algorithm efficiently simulates open quantum systems. *Sci. Rep.* **2016**, *6*, 30727. [[CrossRef](#)] [[PubMed](#)]
37. Cleve, R.; Wang, C. Efficient Quantum Algorithms for Simulating Lindblad Evolution. *arXiv* **2016**, arXiv:1612.09512.

38. Jo, M.; Kim, M. Simulating open quantum many-body systems using optimised circuits in digital quantum simulation. *arXiv* **2022**, arXiv:2203.14295.
39. Ciccarello, F.; Lorenzo, S.; Giovannetti, V.; Palma, G.M. Quantum collision models: Open system dynamics from repeated interactions. *Phys. Rep.* **2022**, *954*, 1–70. [[CrossRef](#)]
40. Algaba, M.G.; Ponce-Martinez, M.; Munuera-Javaloy, C.; Pina-Canelles, V.; Thapa, M.; Taketani, B.G.; Leib, M.; de Vega, I.; Casanova, J.; Heimonen, H. Co-Design quantum simulation of nanoscale NMR. *arXiv* **2022**, arXiv:2202.05792. [[CrossRef](#)]
41. Rabi, I.I. On the Process of Space Quantization. *Phys. Rev.* **1936**, *49*, 324–328. [[CrossRef](#)]
42. Rabi, I.I. Space Quantization in a Gyration Magnetic Field. *Phys. Rev.* **1937**, *51*, 652–654. [[CrossRef](#)]
43. Bloch, F.; Siegert, A. Magnetic Resonance for Nonrotating Fields. *Phys. Rev.* **1940**, *57*, 522–527. [[CrossRef](#)]
44. Jaynes, E.; Cummings, F. Comparison of quantum and semiclassical radiation theories with application to the beam maser. *Proc. IEEE* **1963**, *51*, 89–109. [[CrossRef](#)]
45. Cummings, F.W. Reminiscing about thesis work with ET Jaynes at Stanford in the 1950s. *J. Phys. B At. Mol. Opt. Phys.* **2013**, *46*, 220202. [[CrossRef](#)]
46. Xie, Q.; Zhong, H.; Batchelor, M.T.; Lee, C. The quantum Rabi model: Solution and dynamics. *J. Phys. A Math. Theor.* **2017**, *50*, 113001. [[CrossRef](#)]
47. Forn-Díaz, P.; Lisenfeld, J.; Marcos, D.; García-Ripoll, J.J.; Solano, E.; Harmans, C.J.P.M.; Mooij, J.E. Observation of the Bloch-Siegert Shift in a Qubit-Oscillator System in the Ultrastrong Coupling Regime. *Phys. Rev. Lett.* **2010**, *105*, 237001. [[CrossRef](#)] [[PubMed](#)]
48. Niemczyk, T.; Deppe, F.; Huebl, H.; Menzel, E.P.; Hocke, F.; Schwarz, M.J.; Garcia-Ripoll, J.J.; Zueco, D.; Hümmer, T.; Solano, E.; et al. Circuit quantum electrodynamics in the ultrastrong-coupling regime. *Nat. Phys.* **2010**, *6*, 772–776. [[CrossRef](#)]
49. Braumüller, J.; Marthaler, M.; Schneider, A.; Stehli, A.; Rotzinger, H.; Weides, M.; Ustinov, A.V. Analog quantum simulation of the Rabi model in the ultra-strong coupling regime. *Nat. Commun.* **2017**, *8*, 779. [[CrossRef](#)] [[PubMed](#)]
50. Forn-Díaz, P.; García-Ripoll, J.J.; Peropadre, B.; Orgiazzi, J.L.; Yurtalan, M.A.; Belyansky, R.; Wilson, C.M.; Lupascu, A. Ultrastrong coupling of a single artificial atom to an electromagnetic continuum in the nonperturbative regime. *Nat. Phys.* **2016**, *13*, 39–43. [[CrossRef](#)]
51. Yoshihara, F.; Fuse, T.; Ashhab, S.; Kakuyanagi, K.; Saito, S.; Semba, K. Superconducting qubit-oscillator circuit beyond the ultrastrong-coupling regime. *Nat. Phys.* **2016**, *13*, 44–47. [[CrossRef](#)]
52. Langford, N.K.; Sagastizabal, R.; Kounalakis, M.; Dickel, C.; Bruno, A.; Luthi, F.; Thoen, D.J.; Endo, A.; DiCarlo, L. Experimentally simulating the dynamics of quantum light and matter at deep-strong coupling. *Nat. Commun.* **2017**, *8*, 1715. [[CrossRef](#)]
53. Lv, D.; An, S.; Liu, Z.; Zhang, J.N.; Pedernales, J.S.; Lamata, L.; Solano, E.; Kim, K. Quantum Simulation of the Quantum Rabi Model in a Trapped Ion. *Phys. Rev. X* **2018**, *8*, 021027. [[CrossRef](#)]
54. Crespi, A.; Longhi, S.; Osellame, R. Photonic Realization of the Quantum Rabi Model. *Phys. Rev. Lett.* **2012**, *108*, 163601. [[CrossRef](#)] [[PubMed](#)]
55. Todorov, Y.; Andrews, A.M.; Sagnes, I.; Colombelli, R.; Klang, P.; Strasser, G.; Sirtori, C. Strong Light-Matter Coupling in Subwavelength Metal-Dielectric Microcavities at Terahertz Frequencies. *Phys. Rev. Lett.* **2009**, *102*, 186402. [[CrossRef](#)] [[PubMed](#)]
56. Günter, G.; Anappara, A.A.; Hees, J.; Sell, A.; Biasiol, G.; Sorba, L.; Liberato, S.D.; Ciuti, C.; Tredicucci, A.; Leitenstorfer, A.; et al. Sub-cycle switch-on of ultrastrong light-matter interaction. *Nature* **2009**, *458*, 178–181. [[CrossRef](#)] [[PubMed](#)]
57. Lindblad, G. On the generators of quantum dynamical semigroups. *Commun. Math. Phys.* **1976**, *48*, 119–130. [[CrossRef](#)]
58. Gorini, V. Completely positive dynamical semigroups of N-level systems. *J. Math. Phys.* **1976**, *17*, 821. [[CrossRef](#)]
59. Ritsch, H.; Domokos, P.; Brennecke, F.; Esslinger, T. Cold atoms in cavity-generated dynamical optical potentials. *Rev. Mod. Phys.* **2013**, *85*, 553–601. [[CrossRef](#)]
60. Reiserer, A.; Rempe, G. Cavity-based quantum networks with single atoms and optical photons. *Rev. Mod. Phys.* **2015**, *87*, 1379–1418. [[CrossRef](#)]
61. Fabre, C.; Sandoghdar, V.; Treps, N.; Cugliandolo, L.F. (Eds.) *Quantum Optics and Nanophotonics*; Oxford University Press: Oxford, UK, 2017. [[CrossRef](#)]
62. Di Matteo, O.; McCoy, A.; Gysbers, P.; Miyagi, T.; Woloshyn, R.M.; Navrátil, P. Improving Hamiltonian encodings with the Gray code. *Phys. Rev. A* **2021**, *103*, 042405. [[CrossRef](#)]
63. Hatano, N.; Suzuki, M. Finding Exponential Product Formulas of Higher Orders. In *Quantum Annealing and Other Optimization Methods*; Springer: Berlin/Heidelberg, Germany, 2005; pp. 37–68. [[CrossRef](#)]
64. Berry, D.W.; Ahokas, G.; Cleve, R.; Sanders, B.C. Efficient Quantum Algorithms for Simulating Sparse Hamiltonians. *Commun. Math. Phys.* **2006**, *270*, 359–371. [[CrossRef](#)]
65. Aleksandrowicz, G.; Alexander, T.; Barkoutsos, P.; Bello, L.; Ben-Haim, Y.; Bucher, D.; Cabrera-Hernández, F.J.; Carballo-Franquis, J.; Chen, A.; Chen, C.F.; et al. *Qiskit: An Open-Source Framework for Quantum Computing*; CERN: Geneva, Switzerland, 2021. [[CrossRef](#)]
66. Karevski, D.; Platini, T. Quantum Nonequilibrium Steady States Induced by Repeated Interactions. *Phys. Rev. Lett.* **2009**, *102*, 207207. [[CrossRef](#)] [[PubMed](#)]
67. Jozsa, R. Fidelity for Mixed Quantum States. *J. Mod. Opt.* **1994**, *41*, 2315–2323. [[CrossRef](#)]
68. Johansson, J.; Nation, P.; Nori, F. QuTiP 2: A Python framework for the dynamics of open quantum systems. *Comput. Phys. Commun.* **2013**, *184*, 1234–1240. [[CrossRef](#)]

69. Bravyi, S.; Sheldon, S.; Kandala, A.; McKay, D.C.; Gambetta, J.M. Mitigating measurement errors in multiqubit experiments. *Phys. Rev. A* **2021**, *103*, 042605. [[CrossRef](#)]
70. Georgopoulos, K.; Emary, C.; Zuliani, P. Modeling and simulating the noisy behavior of near-term quantum computers. *Phys. Rev. A* **2021**, *104*, 062432. [[CrossRef](#)]
71. Ursell, H.D. The evaluation of Gibbs' phase-integral for imperfect gases. *Math. Proc. Camb. Philos. Soc.* **1927**, *23*, 685–697. [[CrossRef](#)]
72. Percus, J.K. Correlation inequalities for Ising spin lattices. *Commun. Math. Phys.* **1975**, *40*, 283–308. [[CrossRef](#)]
73. Shlosman, S.B. Signs of the Ising model Ursell functions. *Commun. Math. Phys.* **1986**, *102*, 679–686. [[CrossRef](#)]
74. IBM. *Qiskit Dokumentation*; IBM: Armonk, NY, USA, 2022.
75. IBM. *IBMQ Devices*; IBM: Armonk, NY, USA, 2022.